



Evaluation of characteristics of raw tea waste-derived adsorbents for removal of metals from aqueous medium

Ayten Ateş¹ · Yasemin Mert¹ · Michael T. Timko²

Received: 9 April 2021 / Revised: 18 June 2021 / Accepted: 29 June 2021 / Published online: 23 July 2021
© The Author(s), under exclusive licence to Springer-Verlag GmbH Germany, part of Springer Nature 2021

Abstract

Chemical modification and microwave activation are cost-effective and eco-friendly engineering methods to improve biochar's physicochemical and adsorption performance. Therefore, a series of biochars samples was produced by pyrolysis at 500 °C in the presence of phosphoric acid (H₃PO₄) without and with microwave (MW) irradiation of the raw tea waste (RTW). Effect of acid and MW activation on the characteristics of biochar was compared with biochars produced from pyrolysis of RTW at 300, 500, 700, and 900 °C. Pyrolysis in the presence of H₃PO₄ promoted the formation of oxygen-containing functional groups and increased the surface area of the biochar product (931 m² g⁻¹ compared with 13.6 m² g⁻¹). Compared with biochars obtained from acid-assisted pyrolysis, MW activation nearly doubled the measured surface area (1763 m² g⁻¹) by the formation of a micropore structure and required seconds instead of hours to perform. Heavy metal adsorption capacities observed for the acid-activated chars were comparable to biochar samples produced in the temperature range of 500–900 °C, but acid-promoted activation required much lower temperatures, and the effects of activation depended on the metal, the solution pH, and the activation treatment. Specifically, acid promotion increased Cu and Cd sorption capacity, attributable to the increased surface area and increased surface densities of oxygen functional groups (C=O and OH). The results of ternary-metal adsorption results demonstrated the competitive adsorption between three metals, and the affinity sequence of biochar produced at 900 °C (BC900) was found as Pb(II) > Cd(II) > Cu(II). However, the metal affinity sequence of BC900 to single metal is Pb(II) > Cu(II) > Cd(II). FTIR and SEM–EDS results revealed that Pb(II) had the same adsorption sites with Cu(II), but Pb(II) has a greater affinity than Cu(II). Kinetic measurements and spectroscopic analysis indicated that Pb, Cu, and Cd form chemical complexes on the surface. These results provide new insight on the utilization of tea wastes for heavy metal removal from aqueous streams.

Keywords Raw tea waste · Pyrolysis · Microwave irradiation · Acid activation · Biochar · Heavy metal

1 Introduction

Biochar is the carbonaceous solid product formed from the thermochemical conversion of biomass in the presence of sub-stoichiometric oxygen concentrations. Biochar has been proposed for soil improvement, carbon sequestration, pollution control, energy production, and other applications [1–3]. Pore network, surface area, and the density and types of surface functional groups present on the biochar surface

determine its performance for these different applications. In turn, these textural, structural, and chemical properties depend on the biomass feedstock characteristics and the pyrolysis operating conditions, including heating rate, reaction temperature, reaction time, type and flow rate of carrier gas, the presence of catalyst, or additives [4].

Biochar has recently received considerable attention as a renewable material for removal of heavy metals from the environment [5] because of its relatively low cost (c.f., \$246 ton⁻¹) [6] and the abundance of biomass materials produced as agricultural and forestry wastes. The characteristics of the biochar such as the carbon richness, high porosity and large surface area, and presence of the various functional groups (hydroxyl, carboxyl, alkyl, phenolic, and amino groups) provide a great level of attraction/affinity for adsorption of

✉ Ayten Ateş
ates@cumhuriyet.edu.tr

¹ Department of Chemical Engineering, Sivas Cumhuriyet University, Engineering Faculty, 58140 Sivas, Turkey

² Department of Chemical Engineering, Worcester Polytechnic Institute, Worcester, MA 01609, USA

metal ions (Ni, Co, Hg, Cr, Cu, Zn, Cd, Mn, and Pb) from contaminated water [7].

Despite promise, biochar adsorption capacity is not competitive with most activated carbons. To improve adsorption capacity, biochar has been modified by various physical and chemical methods [8], with the targets typically being to increase surface oxygen functional groups, surface area, and pore volume. Physical activation is performed under oxidizing gas environments such as CO₂ or steam at high temperatures (> 800 °C) [9]. Chemical activation typically involves impregnation of the biochar with solution containing either strong alkali (KOH, NaOH) or acidic components (H₃PO₄, HNO₃), followed by carbonization at 450–900 °C [10]. Chemical modifications such as magnetic treatment with FeCl₃ and impregnation with metal ions, such as ZnCl₂ or KMnO₄ have been used to confer desirable properties in biochar, such as recoverability [11, 12].

Both physical and chemical activation methods increase the degree of aromatic condensation present in biochar and improve its porosity and surface area. Chemical activation proceeds at lower temperatures and faster rates than physical activation [13], yet the requirement of a chemical activating agent is a potential drawback. Among the various activation agents that have been reported to date, phosphoric acid (H₃PO₄) treatment has several advantages: effectiveness at relatively low pyrolysis temperature, low corrosivity, minimal co-production of waste pollutants, and low cost [14]. Also, H₃PO₄ activation may enhance biochar thermal stability and surface acidity by the formation of oxygen–phosphorus surface groups [15] while simultaneously improving its pore structure [16].

H₃PO₄ treatment has been used to activate biochars produced from several different sources with good results. For example, Fernandez et al. (2015) studied H₃PO₄ activation of orange peel biochar, reporting improved sorption capacity for organic contaminants [17]. Wu et al. (2017) showed that H₃PO₄ treatment of pomelo peel biochar produced at 450 °C increased its Cr(VI) sorption capacity [18]. Taha et al. (2014) studied biochars obtained from rice straw biochar (BRc) and corn stover biochar (BCn) after and before H₃PO₄ treatment for pesticide from aqueous solution and found that H₃PO₄ treatment significantly increased the surface functional group densities and aromatization for all of the treated adsorbents [19].

Microwave irradiation offers distinct advantages compared with pyrolysis as its rapid and uniform heating results in greater retention of polynuclear aromatic hydrocarbon (PAH) than conventional heating [20, 21]. Therefore, microwave heating has the potential to produce biochar with favorable properties compared with those produced through conventional pyrolysis, potentially with much less energy use and much shorter time scales of seconds compared with hours [22]. Liu et al. (2010) reported the synthesis of active

carbon from bamboo using H₃PO₄ as a chemical activation agent and microwave heating [23]. They reported the transition of micropore to mesopore structure when irradiated at 400 W, ascribing their finding to a vigorous reaction between carbon and H₃PO₄ at these conditions. Yagmur et al. (2008) studied microwave-promoted pyrolysis of tea waste for the production of activated carbon impregnated with excess H₃PO₄ (H₃PO₄:tea waste = 3:1), finding a maximum surface area of 1157 m²g⁻¹ at optimal conditions [24].

Previous works suggest that both H₃PO₄ and microwave promotion have potential for the production of activated carbon-type materials with favorable surface area and adsorption properties [25–27]. However, a major challenge is isolating the benefits of H₃PO₄ and microwave activations and understanding if similar effects can be obtained simply by optimizing pyrolysis temperature. Without this knowledge, optimal conversion of waste feeds to valuable carbonaceous solids requires trial-and-error study.

Tea has been produced as an agricultural product by many countries including China, India, Sri Lanka, Kenya, Vietnam, and Indonesia [28]. Annual tea production in the world was reported as almost 5.73 million tons in 2016, and large amounts of tea waste were also produced [28]. For example, about 18% of total tea production is results in waste generation [29], causing a solid waste disposal problem. Tea waste mainly involves cellulose, hemicellulose, and lignin along with polyphenols, proteins, vitamins, amino acids, major elements, and trace elements [30], providing an opportunity as an ideal feedstock, being widely available and low cost.

Given the abundance of tea waste, the development of new methods for its utilization is essential. Among these methods, biochar production for different applications has been studied previously, including fuel production [31], energy storage [30], and use as an adsorbent to remove various pollutants from aqueous solutions, gases and sediments including sulfamethazine [32], ciprofloxacin [33], 2,4-D [34], carbofuran [35], caffeine [36] elemental mercury [37], fluoride [38], phosphate [39], and Cd [40, 41].

Based on the aforementioned studies, conversion of RTW to biochar to obtain new carbonaceous materials with specific physiochemical characteristics was evaluated.

RTW was selected as the feed due to its abundance, as approximately 40,000 tons of RTW are produced each year by the tea factories around the Eastern Black Sea of Turkey, and lack of viable options for its valorization [42]. Specifically, the effect of activation with H₃PO₄ and microwave (MW) irradiation in the presence of H₃PO₄ on the biochar characteristics was determined. Despite studies reported in the literature, here, the aim of MW irradiation is activation of raw tea waste within a very short time, rather than the hours of activation required by the energy intensive pyrolysis activation method. To compare with acid and MW activation, biochars were produced by conventional pyrolysis over

the temperature range from 300 to 900 °C. After comparing the properties and characteristics of these different biochar adsorbents, Cd, Cu, and Pb were studied as model adsorbates to study the adsorption capacities of new porous biochar materials to be further used in the removal of heavy metal pollutants from aqueous solution. The present results provide new guidelines for selection of activation processes that optimize adsorption performance.

2 Experimental method

2.1 Materials

Raw tea waste (RTW) was obtained from a tea plant located in Salarha, Rize, Turkey. The RTW was ball-milled to particle size, ranging from 0.25 to 0.5 mm, and oven-dried at 100 °C for 12 h. The moisture content of samples was determined by weight loss at 105 °C at an air gas rate of 25 mL/min. Ash content of samples was performed by heating of samples (1.0 g) at 900 °C for 8 h in the air, and ash content was calculated from differences between initial and final sample mass. Volatile matter was determined by heating samples in a crucible with lid to 900 °C in a limited oxygen environment, holding it for 10 min. Amount of volatile matter was the difference between the initial mass and final mass. Fixed carbon (FC) amount of samples is calculated by Eq. (1). Volatile matter contains humidity of samples. The results obtained are listed in Table 1.

$$\% \text{ Fixed Carbon (FC)} = 100 - (\text{volatile matter \%} + \text{ash \%}) \quad (1)$$

Metal solutions were prepared using 1000 mg L⁻¹ of Pb²⁺ as Pb(NO₃)₂ (Carlo Erba), Cd²⁺ as Cd(NO₃)₂ (Merck), and Cu²⁺ as Cu(NO₃)₂•3H₂O (Merck). HCl and NaOH solutions were used to adjust pH.

2.2 Biochar production and characterization

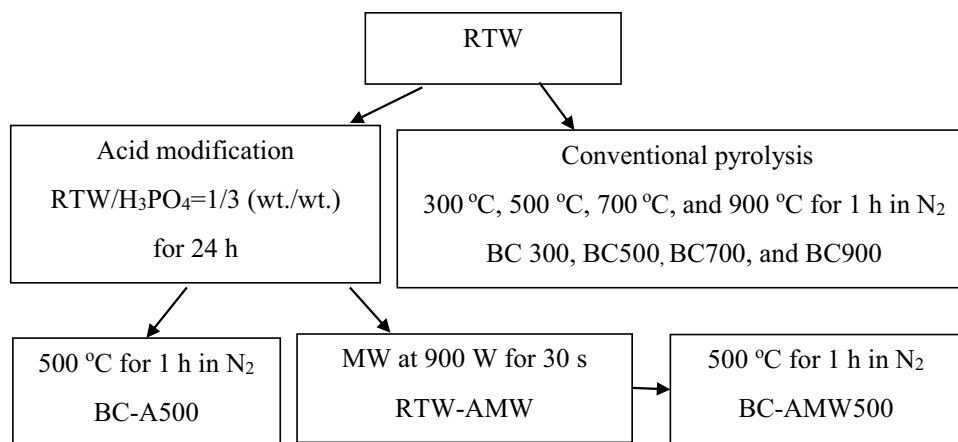
The production schematic diagram of biochar from RTW is summarized in Fig. 1. The dried biomass was pyrolyzed at 300, 500, 700, and 900 °C with a heating rate of 10 °C min⁻¹ for 1 h under N₂ (80 cm³ min⁻¹) using a quartz reactor (20 mm I.D) in a Protherm split furnace shown in Fig. S1. Pyrolyzed tea wastes, biochar (BC) are denoted as BCx, where “x” indicates pyrolytic temperature. For H₃PO₄ activation, 2 g of the RTW was mixed with 6 g of 85 wt% H₃PO₄ (Merck) in PTFE® containers and then subjected to microwave (MW) irradiation in a digestion system (Cem Mars 6) for 30 s. The input power of the MW equipment was 900 W, and the frequency was 2.45 GHz. After MW activation in acid, the sample was dried in air. H₃PO₄-MW activated samples are denoted as RTW-AMW where A indicates the presence of acid and MW refers to microwave irradiation. After MW activation, the sample was pyrolyzed at 500 °C for 1 h under 80 cm³ min⁻¹ N₂ flow. Samples are denoted as BC-AMW500 to specify MW activation in acid and pyrolysis at 500 °C. For comparison with BC-AMW500, the RTW was mixed with H₃PO₄ under the same conditions as before and pyrolyzed at 500 °C for 1 h under 80 cm³ min⁻¹ N₂ flow without MW treatment. This sample is denoted as BC-A500. All samples produced in the presence of phosphoric acid were washed several times with distilled water to the removal of phosphate species.

Table 1 Compositions of samples (wt%) determined by an elemental analyzer before and after adsorption from solutions containing 50 mg/L of Pb²⁺, Cd²⁺, and Cu²⁺

Sample	Humidity % (wt)	Ash % (wt)	Volatile % (wt)	FC % (wt)	Yield % (wt)	C+H	C	O	N	H	S	H/C (mol/mol)	O/C (mol/mol)	(O+N)/C (mol/mol)
RTW	2.8	2.0	91.3	6.7	-	47.8	45.3	45.6	2.6	6.4	0.1	1.70	0.75	0.80
RTW-AMW	12.2	2.7	78.2	19.1	42.2	62.3	54.1	40.9	1.5	3.3	0.1	0.73	0.57	0.59
BC-A500	3.7	11.9	55.0	33.1	48.8	80.1	69.2	28.2	0.5	2.1	n.d	0.36	0.31	0.31
BC-AMW500	2.7	11.8	31.5	56.4	47.0	58.8	67.5	30.0	0.7	1.7	n.d	0.30	0.33	0.34
BC300	3.6	5.6	68.3	26.0	48.0	54.9	60.7	33.5	2.7	5.1	0.1	1.01	0.41	0.45
BC500	4.5	8.2	47.1	44.7	31.0	72.4	68.2	26.2	2.5	2.9	0.1	0.51	0.29	0.32
BC700	4.3	10.9	41.7	47.4	29.4	70.7	69.5	26.7	2.1	1.5	0.2	0.26	0.29	0.31
BC900	4.0	12.8	39.4	47.8	28.1	69.0	72.5	24.9	1.8	0.7	n.d	0.12	0.26	0.28
BC900-Pb	-	-	-	-	-	87.8	72.5	24.8	1.8	0.7	n.d	0.12	0.26	0.28
BC900-Cd	-	-	-	-	-	-	74.4	22.8	2.0	0.7	n.d	0.11	0.23	0.25
BC900-Cu	-	-	-	-	-	-	79.2	17.8	2.2	0.7	n.d	0.11	0.17	0.19

n.d: Not detected.

Fig. 1 Production diagram of biochar from RTW



Elemental composition (C, H, N, and S) of RTW and the various carbonaceous products was determined by an elemental analyzer (Thermo Scientific & Flash 2000/MAS 200R), and oxygen (O) content of samples was calculated by mass balance. Elemental composition results are the average of measurements obtained from two measurements. The pH of samples was determined by preparing a suspension of a sample (1:100 w/v) in de-ionized water, followed by analyzing using a digital pH meter (ThermoFisher Scientific Inc., Waltham, MA, USA). X-ray powder diffraction (XRD) patterns of the samples were recorded on a Rigaku SmartLab X-ray diffractometer using non-monochromotographic Cu K α 1 radiation (40 kV, 40 mA, $\lambda = 1.5 \text{ \AA}$). Scanning was in the 2θ range of $5\text{--}65^\circ$. Surface functional groups were characterized by Fourier transform infrared spectroscopy (FT-IR) (Bruker Tensor II). The FT-IR measurements were performed by mixing the sample with KBr (sample: KBr = 1:100, w/w) in the wavenumber range of $400\text{--}4000 \text{ cm}^{-1}$. A background spectrum was obtained using a pure KBr pellet. Surface morphologies of all samples were examined using a field emission scanning electron microscope (TESCON-Mira III XMU) equipped with EDS (Oxford Inst. INCA). Brunauer–Emmett–Teller (BET) specific surface area (S_{BET}), total pore volume, and average pore diameter were determined using a gas sorption analyzer (AUTOSORB 1C, Quantachrome Corp., USA).

Differential scanning calorimetry (DSC) of samples was carried out using a DSC (DSC 60, Shimadzu, Japan) instrument with TS-60WS software interface. About 5 mg of samples were put into aluminum pans and pressed. The sample was heated at a constant heating rate of $10 \text{ }^\circ\text{C}/\text{min}$ from 35 to $550 \text{ }^\circ\text{C}$ under a flowing N_2 ($25 \text{ cm}^3 \text{ min}^{-1}$).

Zeta potential measurements were determined using a zeta meter (Malvern Zetasizer Nano-Z). For each test, 0.005 g of the sample was suspended in 100 cm^3 of de-ionized water followed by homogenization for 2 h in an ultrasonic bath. After ultra-sonication, the aqueous suspension

was equilibrated at different pH values for 30 min. Zeta results obtained are an average of three measurements.

2.3 Batch adsorption experiments

Adsorption of Pb^{2+} , Cd^{2+} , Cu^{2+} , and their mixtures was studied in a batch system. Single metal adsorption studies were performed at a single concentration of 50 mg L^{-1} at initial pH values of 3.0, 7.0, and 9.0. Ternary metal adsorption studies were carried out in the concentration range of $50\text{--}150 \text{ mg L}^{-1}$ at $\text{pH} = 4$. The adsorbent loading was 1 g L^{-1} for all adsorption experiments, and samples were equilibrated for 6 h after preliminary tests indicated that this was sufficient. Adsorption experiments were performed at $25 \text{ }^\circ\text{C}$ while being mixed at 200 rpm in a magnetic shaker (IKA-RT10). The resulting mixtures were filtered using $0.45 \text{ }\mu\text{m}$ nylon syringe disposable filters (Chrom Xpert), and supernatant liquids were kept in plastic centrifuge tubes prior to analysis using ICP-MS (Thermo Scientific iCAP Q Series ICP-MS). After adsorption, the carbon dissolved from biochar samples was determined by total organic carbon analyzer (Shimadzu, TOC-LCPN (SSM-5000A/ASI)). All results are expressed as average values obtained from duplicate tests. The adsorbents used in adsorption tests were dried in air under ambient conditions and stored for further analysis (SEM–EDS and FT-IR). The metal adsorption capacity (q_e , mg g^{-1}) was determined using the following equation:

$$q_e = \frac{(C_o - C_e)V}{m} \quad (2)$$

where C_o and C_e are the initial and final concentrations of metals (mg L^{-1}), respectively, V is the volume of solution (L), and m is the amount of adsorbent (g).

Kinetic studies were performed at $25 \text{ }^\circ\text{C}$ on the BC900 sample for removal of Pb^{2+} and Cu^{2+} at $\text{pH} = 4.0$ and Cd^{2+} at $\text{pH} = 7$ based on ionic stability of metal ions. For each test,

the supernatant liquid was extracted at regular time intervals and analyzed for metal content using ICP-MS, as before.

3 Results and discussion

3.1 Characterization results

3.1.1 Composition of samples

Table 1 lists the elemental analysis results of all samples. Carbon and oxygen are abundant constituents of all of these materials; their combination always accounts for at least 90% of the material. Nitrogen is the next most abundant element, typically accounting for 2.6% of the material. In addition, RTW contains 0.1% S along with traces of Al, Cl, K, Ca, Na, and Mg as seen in Table S1. The RTW involves volatile matter (91.3 wt%) and fixed carbon (6.7 wt%) with small amounts of moisture (2.8 wt%) and ash (2.0 wt%).

Pyrolysis decreased the oxygen and hydrogen content and increased the carbon content of the materials, attributable to release of CO_2 via decarboxylation and depolymerization and H_2O via dehydration reactions [43, 44] (Table 1 and Fig. 2). Similarly, nitrogen content decreased slightly after pyrolysis. Removal of nitrogen is consistent with deamination reactions [45] resulting in the liberation of HCN and NH_3 gases. At 300 °C, the RTW was partially pyrolyzed, and the resulting biochar contains a mixture of biochar and unpyrolyzed RTW containing the more thermally stable compounds such as cellulose and lignin that convert into

volatiles and the char at a temperature higher than 300 °C [46]. By increasing pyrolysis temperature from 300 to 900 °C, the C content increased from 60.7 to 70.5%, and O, H, and N contents decreased from 33.5 to 24.5%, from 5.1 to 1.8%, and from 2.7 to 1.8%, respectively. To characterize biochar yielded from the RTW, Van Krevelen plots are drawn using elemental analysis results in Table 1 [47]. A linear correlation ($R^2=0.92$) between H/C and O/C molar ratios for biochars (Fig. 2) produced was determined.

The slope for H/C-O/C relation is 3.02, which is related to raw material properties [48], allowing us to predict the composition of biochar with pyrolysis temperature. Moreover, the H/C and O/C ratios give information about aromaticity and stability of biochar. For this, Schimmelpfenning et al. reported that the biochar with $\text{H/C} < 0.6$ and $\text{O/C} < 0.4$ shows long-term C sequestration [48]. Results in Table 1 and Fig. 2 show that the biochar samples pyrolyzed ranging from 500 to 900 °C have these H/C and O/C ratios and these values decrease with increasing pyrolysis temperature. Similarly, the larger values of O/C and (O + N/C) are related to a stronger level of hydrophilicity and polarity, respectively [49]. Values of H/C, O/C, and (O + N)/C decreased with increasing pyrolysis temperature from 300 to 900 °C, consistent with increased aromatization.

MW irradiation in H_3PO_4 of the RTW increased C content and decreased O, H, and N contents. Acid-assisted MW irradiation increased ash and fixed carbon amounts and decreased volatile compounds. Pyrolysis of RTW-AMW at 500 °C showed a similar trend with BC500 for carbon content, but MW-assisted acid treatment decreased slightly the oxygen removal from the sample and increased N, H, and S removal. In addition, ash content and char yield increased with acid-assisted MW irradiation and acid-assisted pyrolysis. The presence of phosphoric acid during pyrolysis at 500 °C insignificantly affected carbon content but decreased prominently H and N content. These findings show that phosphoric acid accelerates the deamination and dehydrogenation reactions and inhibits the decomposition of organic fractions in which the crosslink reaction between these polar fractions and H_3PO_4 , as esterification, leads to the formation of alkenes structure in biochar as reported previously [16, 50]. Irrespective of MW irradiation, the acid treatment of the RTW increased the yield of biochar by partial oxidation of carbon with phosphoric acid.

3.1.2 XRD

Figure 3 shows the XRD patterns of the various RTW and char samples. The characteristic peak at 22.5° shows the (002) plane of cellulose [51, 52] and shoulders at 15° and 16.5° indicate lignin and hemicellulose, respectively [53]. Increasing pyrolysis temperature from 500 to 900 °C leads to the disappearance of lignin and hemicellulose features

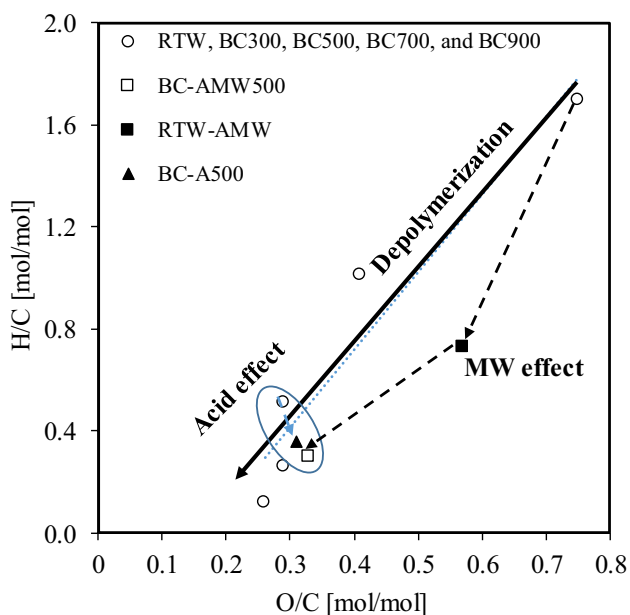


Fig. 2 Van Krevelen diagram for biochars derived from RTW under different pyrolysis temperatures and acid activation

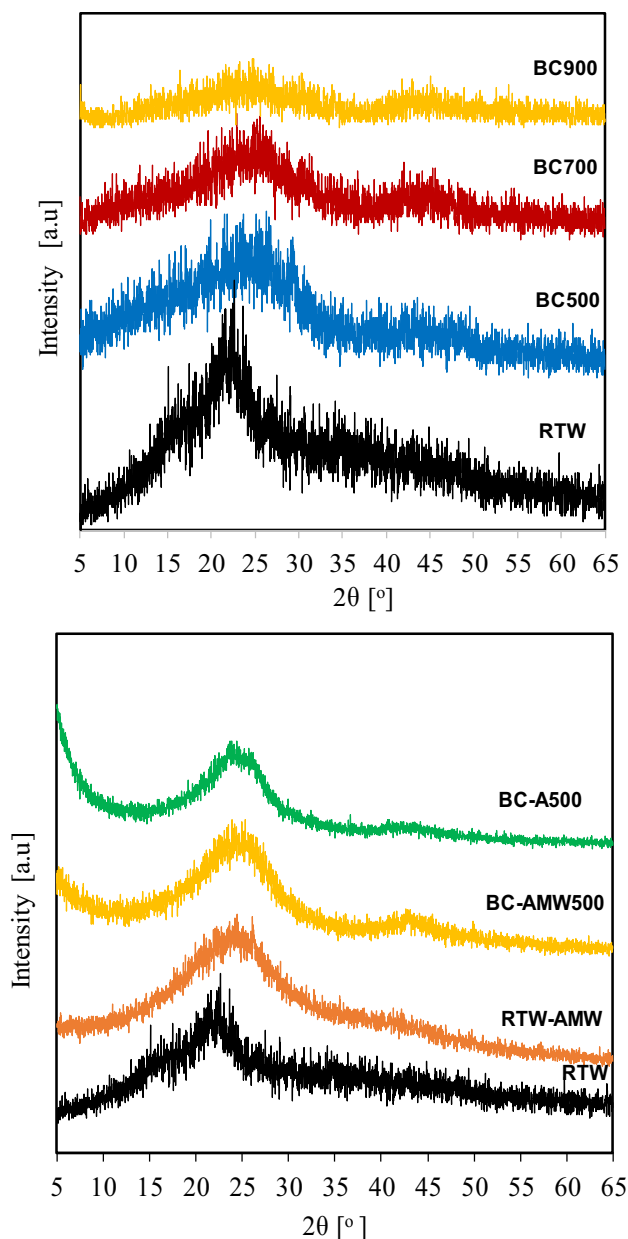


Fig. 3 XRD pattern of RTW, biochar, and acid activated biochars

from the diffractogram, a decrease of cellulose peak attributable to degradation of cellulose, and formation of graphite-like structure of carbon with appearance of a feature centered at $2\theta = 26.5^\circ$ and 43.5° [54]. Acid and MW treatment of RTW removes the shoulder at 15° and decreases intensity of the peak at 22.5° due to the decomposition of hemicellulose, cellulose, and lignin in the presence of acid. Similarly, pyrolysis of RTW-AMW at 500°C and the pyrolysis of the RTW in the presence of phosphoric acid at 500°C lead to the formation of graphite-like carbon and removal of hemicellulose and lignin as seen in Fig. 3.

3.1.3 SEM images

The surface morphologies of RTW, biochars, and activated biochars were examined using SEM, as illustrated in Fig. 4a. The RTW surface is smooth, with few cracks or voids visible. When the RTW is pyrolyzed at 500°C , the BC500 has cracks and crevices. Increasing pyrolysis temperature to 700 and 900°C increases the microscale roughness of the samples, consistent with the removal of hemicellulose and carbonization of cellulose as seen using XRD. Interestingly, pyrolysis of RTW at 700 and 900°C produce a char with a microscale honeycomb structure, as shown in Fig. 4a.

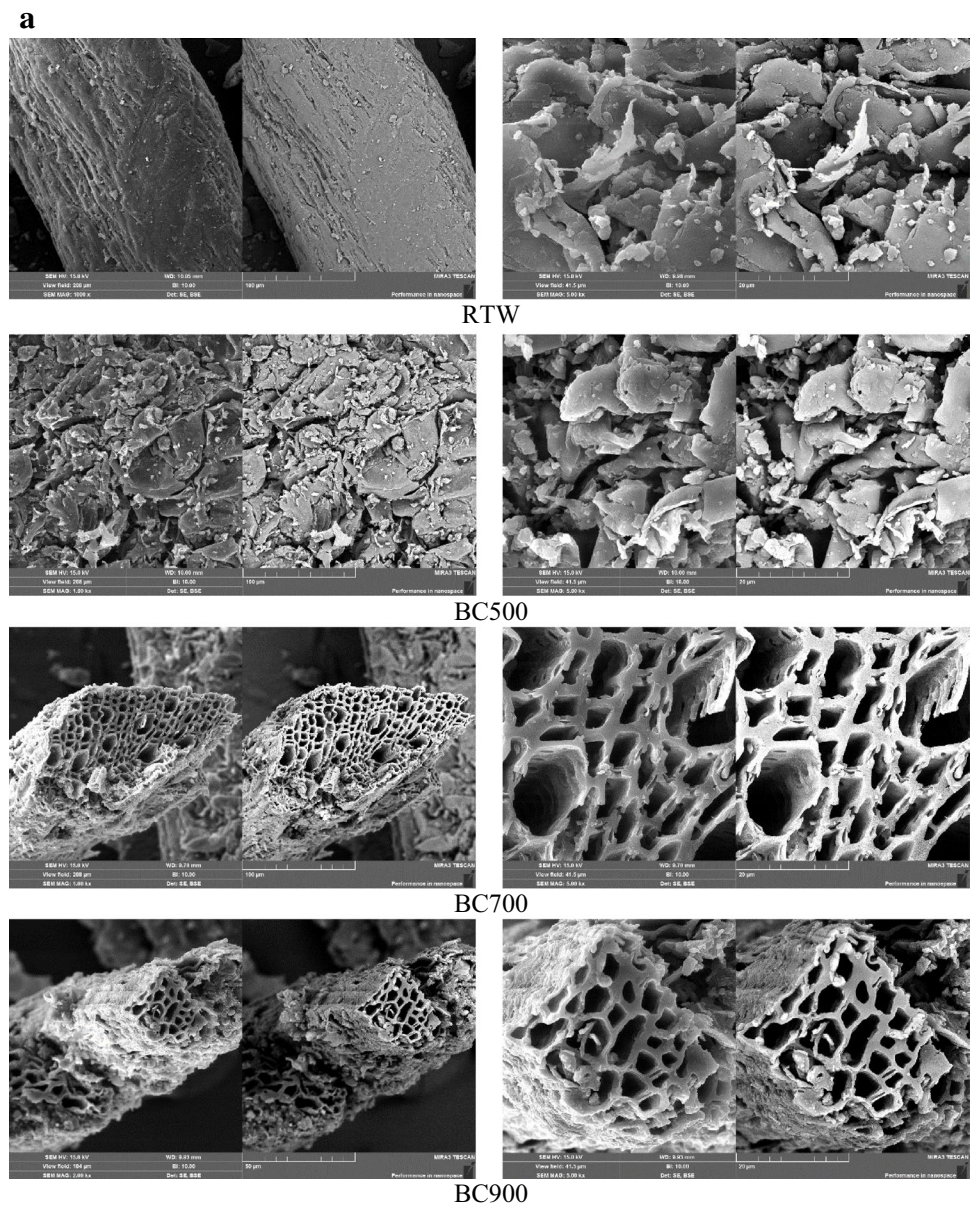
SEM images of samples obtained after MW irradiation and pyrolysis of acid-impregnated RTW are shown in Fig. 4b. MW treatment forms an irregular, heterogeneous surface. The surface of RTW-AMW is pitted, similar to surfaces of acid-treated biomass previously described in the literature [55]. Pyrolysis of RTW-AMW produced a material with a smoother surface compared with the other pyrolysis chars, the result of partial agglomeration of the structure and shrinkage of the pores during carbonization. Pyrolytic treatment of acid-impregnated RTW generated material with a laminated texture consisting of porous surface morphology.

3.1.4 Surface area and pore characteristics

N_2 adsorption–desorption isotherms and the pore size distribution curves of RTW and biochars are shown in Fig. 5. Irrespective of treatment, all samples exhibit type IV isotherm according to the IUPAC classification, indicating a combination of microporous and mesoporous structures and a hysteresis loop associated with capillary condensation taking place in mesopores [56]. The hysteresis loop became more pronounced when pyrolysis temperature was increased from 500 to 900°C , consistent with increased volume of adsorbed nitrogen and increased average diameter of mesopores. The isotherms were fit to determine textural properties, with values provided in Table 2. The surface area and average pore diameter of the RTW and the BC900 are $10.4\text{ m}^2\text{ g}^{-1}$ and 56 \AA and $14.0\text{ m}^2\text{ g}^{-1}$ and 80 \AA , respectively. SEM in Fig. S2 suggests the formation of macropores in the range $6\text{--}15\text{ }\mu\text{m}$ at pyrolytic temperatures $\geq 700^\circ\text{C}$, but N_2 adsorption does not detect them probably due to the abundance of mesopores in these materials.

Figure 5 shows adsorption–desorption isotherms obtained from analyzing samples obtained after pyrolysis and MW activation of the acid impregnated RTW. The presence of acid during pyrolysis greatly increases the surface area of the pyrolyzed product, primarily in the form of increased microporosity (Table 2 and Fig. 5). The average pore diameters of BC-A500 and BC-AMW500 are 23 \AA and 16.6 \AA , respectively. Their pore size distributions in Fig. 4 are in the range of $2.8\text{--}20\text{ \AA}$, indicating that the samples are mostly

Fig. 4 **a** SEM pictures of RTW and biochars produced by pyrolysis of RTW at different temperatures. **b** SEM pictures of samples produced by MW irradiation and pyrolysis in the presence of H_3PO_4



microporous. MW irradiation of the acid impregnated RTW produced only modest increases in microporosity and surface area, an observation that might be attributable to the short microwave times (30 s) as reported by Rey-Raap et al. (2014) [57].

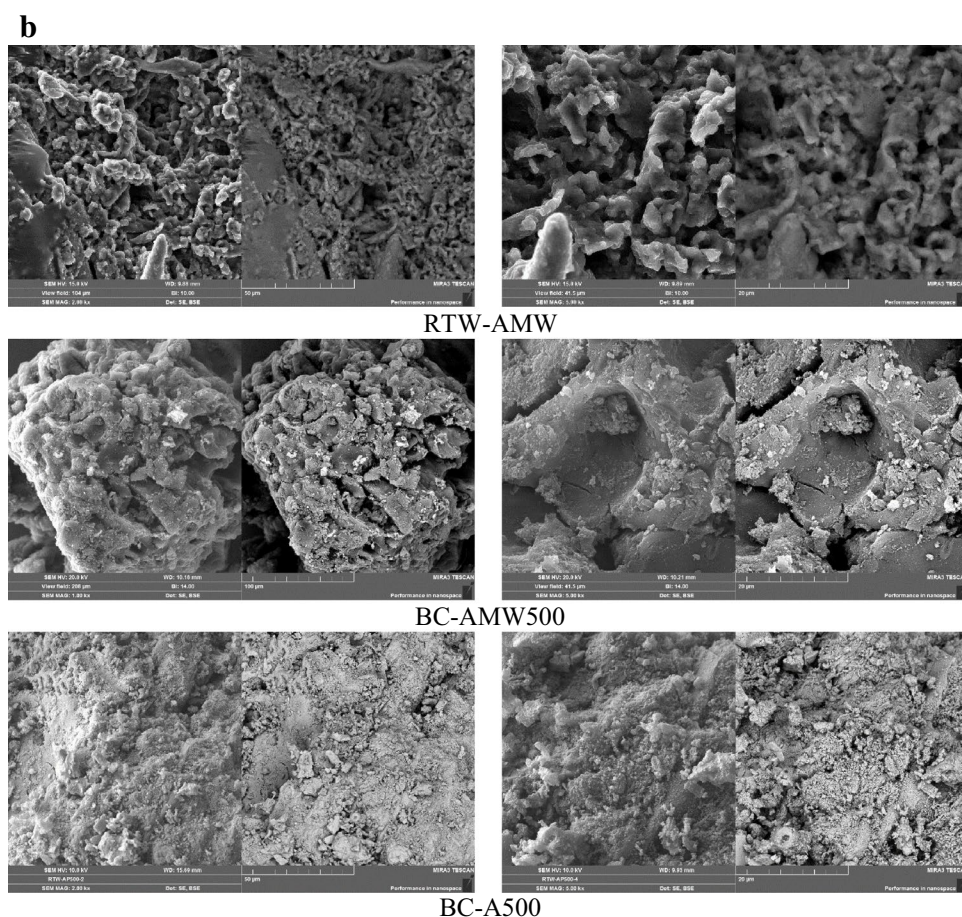
Pyrolysis of the acid-impregnated and MW irradiated sample increased its surface area due to formation of micropores. Specifically, the surface area of BC-AMW500 is nearly two times greater than that of BC-A500, again consistent with a beneficial interaction between acid, MW, and pyrolysis treatments and similar to some previous studies [24, 58–61]. Increased surface area observed after pyrolysis of RTW-AMW is attributable to distortion and formation of inhomogeneous microstructure in the presence of acid and water vapor formed by reaction of oxygen-containing

functional groups with H_3PO_4 [62]. Myglovets et al. (2014) and Sun et al. (2015) reported that reaction of phosphoric acid with carbon ($4H_3PO_4 + 10C \rightarrow P_4 + 10CO + 6H_2O$) creates porous graphene “sheds” that can explain the effect observed for the waste feed studied here [63, 64].

3.1.5 DSC

Figure 6 shows the DSC curves for RTW, biochar, and acid-activated biochar. The negative heat evolution values for RTW are observed between 50 and 150 °C, and these endothermic phenomena could be due to the dehydration and loss of physically adsorbed water and low molecular weight organic compounds [65, 66]. Two endothermic peaks in the BC500 are observed at around 115 and 150 °C, respectively.

Fig. 4 (continued)



In addition, the peak maximums shifted slightly higher temperatures and widened. A single broad peak in BC700 is observed at 97 °C, and a further increase of pyrolysis temperature to 900 °C leads to the formation of a sharp peak at 97 °C. Widening and then narrowing of peaks with pyrolysis could be due to the formation of pores with different size and shapes in the biochar as seen in Fig. 4. The pore distribution and pore diameter are distributed heterogeneously, and increasing pyrolysis temperature leads to the conversion of micro- and mesopores to meso- and macropores as seen in pore characteristics in Table 2 and Figs. 4 and 5.

The treatment and pyrolysis in the presence of phosphoric acid shifted peaks below 200 °C to higher temperatures. Namely, MW treatment in the presence of phosphoric acid leads to shifting of the peak maximum at 97 to 126 °C due to the formation of micropores by dissolution effect of acid as seen in Table 2. After MW treatment in acid, the pyrolysis at 500 °C led to the peaks to narrow and sharpen by opening micropores with pyrolysis. Pyrolysis in the presence of phosphoric acid showed a similar effect to the results of biochar produced after acid-assisted MW, but the shifting at peak maximum is lower. Based on the average pore diameter results in Table 2, MW treatment of RTW in the acid

enhances micropore formation of biochar by the formation of gases and steam released from H_3PO_4 -treated biochars [16, 67, 68]

Three peaks between 250 and 500 °C in RTW are observed. The shoulder between 250 and 315 °C is related to the destruction of the hemicellulose which is the main process in torrefaction in the RTW [69, 70]. The exothermic peak between 315 and 360 °C is assigned to cellulose decomposition in RTW [69]. A broad peak above 360 °C shows the decomposition of lignin, a complex three-dimensional macromolecule. It is reported that its thermal degradation starts at 200 °C and continues up to 900 °C depending on the residence time [69]. These peaks detected in RTW disappeared by pyrolysis irrespective of the presence of acid and MW treatment. This is related to the decomposition of hemicellulose, cellulose, and lignin in the presence of acid and by increasing temperature.

3.1.6 FT-IR

Figure 7a shows FT-IR spectra obtained from analysis of RTW and biochars. The aliphatic C–H stretching band occurs at 2920–2855 cm^{-1} , aromatic carbonyl/carboxyl

Fig. 5 N₂ adsorption–desorption isotherms and pore size distributions of RTW, biochars, and acid activated biochars

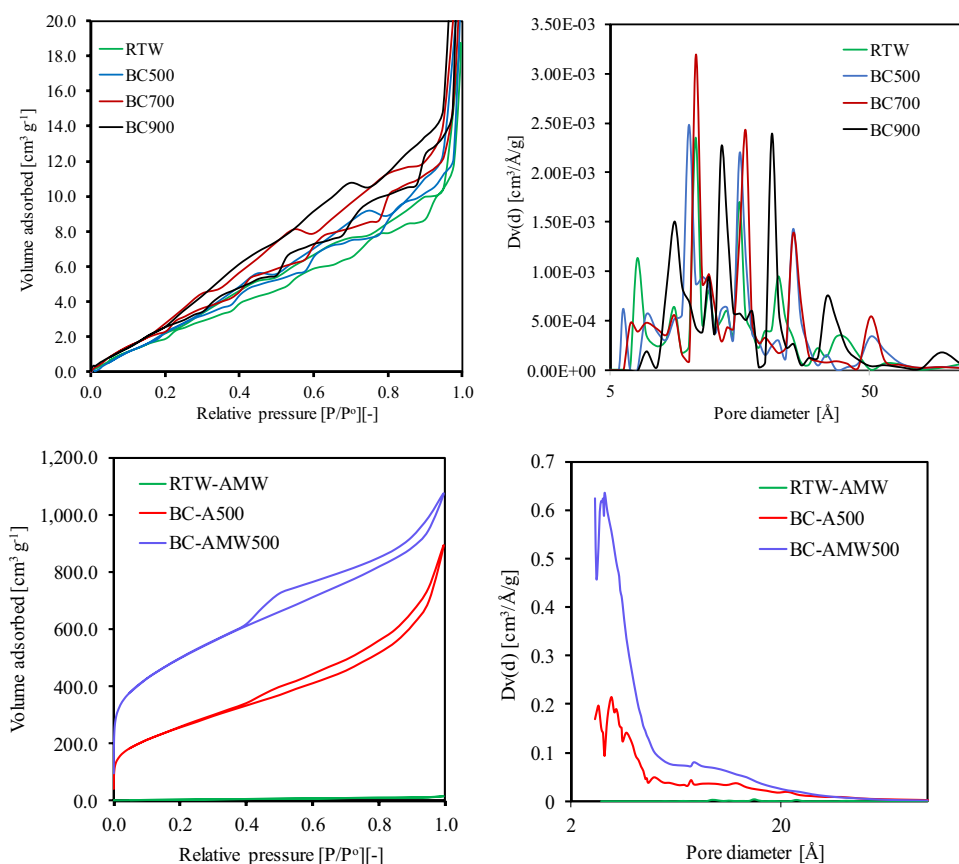


Table 2 Surface area and pore characteristics of RTW, biochars, and acid activated biochars

Sample	$S_{\text{BET}}^{\text{a}}$ (m^2g^{-1})	$V_{\text{Total}}^{\text{b}}$ (cm^3g^{-1})	$V_{\text{Micro}}^{\text{c}}$ (cm^3g^{-1})	Dp^{d} (Å)
RTW	10.4	0.029	0.004	55.6
BC500	13.6	0.035	0.006	51.8
BC700	13.9	0.039	0.012	66.2
BC900	14.0	0.030	0.056	79.9
BC-A500	931	1.080	0.374	23.4
RTW-AMW	18.5	0.018	0.005	19.2
BC-AMW500	1763	1.460	0.764	16.6

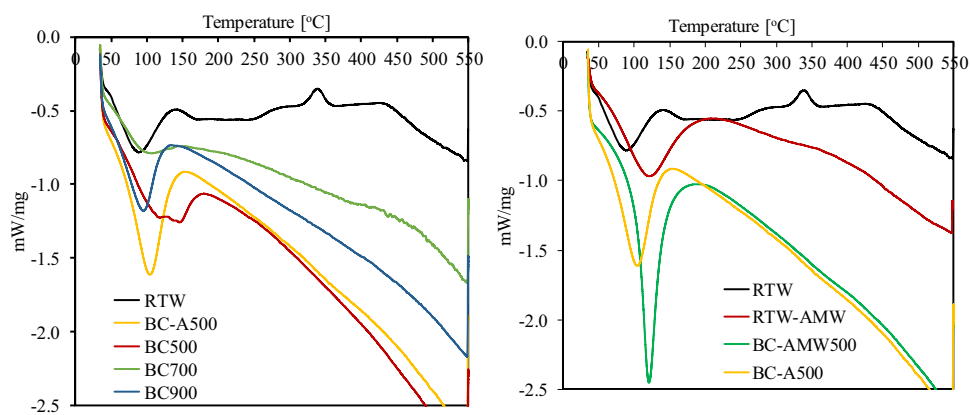
^aSurface area calculated using multiple point BET; ^btotal volume calculated from volume at $P/P_0=0.95$; ^cmicropore volume calculated using the Dubinin-Radushkevich (DR) method; ^dmedium pore diameter calculated using density functional theory (DFT).

C=O at $\sim 1700\text{ cm}^{-1}$ [71, 72], aromatic C=C and C=O stretches at $\sim 1600\text{ cm}^{-1}$, and aliphatic C–O–C and alcohol –OH at $1245\text{--}1050\text{ cm}^{-1}$ [73]. Detailed peak assignments are listed in Table S2. The distribution and intensity of vibrational bands observed in RTW changed significantly with increasing pyrolysis temperature. In RTW, an intense OH stretch was observed at $\sim 3400\text{ cm}^{-1}$, attributable to surface hydroxyl groups. The OH stretching band disappears after pyrolysis, presumably due to dehydroxylation, dehydrogenation, and aromatization of cellulosic and lignin components [74]. In addition, the intensities of bands associated with

C=C in aromatic rings and C–H in methyl and methylene groups decreased, and bands associated with C–H, C=O, C=C, aliphatic C–O–C, and alcohol –OH disappeared after pyrolysis at $500\text{ }^\circ\text{C}$. After pyrolysis at 700 and $900\text{ }^\circ\text{C}$, bands associated with functional groups disappeared due to removal of hemicellulose and lignin, consistent with previously presented XRD diffractograms and DSC results.

Figure 7b provides FT-IR spectra of biochars produced after acid impregnation. After MW activation in the presence of H_3PO_4 , the bands at $1560\text{--}1200\text{ cm}^{-1}$ disappeared, and other bands shifted position: C–O (from 1050 to

Fig. 6 Differential scanning calorimetry analysis results of samples



1100 cm^{-1} , C=O (1742 to 1710 cm^{-1}), and $\text{C}=\text{C}$ (from 1649 to 1612 cm^{-1}). Collectively, these changes indicate structural deformation in the presence of acid. Intensities of OH and CH bands decreased after MW irradiation and disappeared after pyrolysis irrespective of MW activation.

Acid-assisted pyrolysis did not impact C=O, C=C, and C–O features. However, acid treatment followed by MW irradiation decreased the intensities of C–O, C=C, and C=O features due to oxidation and partial decarboxylation and decarbonylation.

A new band appeared at 750 cm^{-1} after acid-assisted pyrolysis, which may represent the symmetric stretch of P–O–P in polyphosphate that cannot be removed by washing (Table S1). Comparing spectra obtained after acid-assisted pyrolysis of RTW (Fig. 7b) with those obtained after conventional pyrolysis (Fig. 7a) shows that acid treatment increases the intensities of features associated with COOH and OH groups, indicating the reaction of carbon with H_3PO_4 [62].

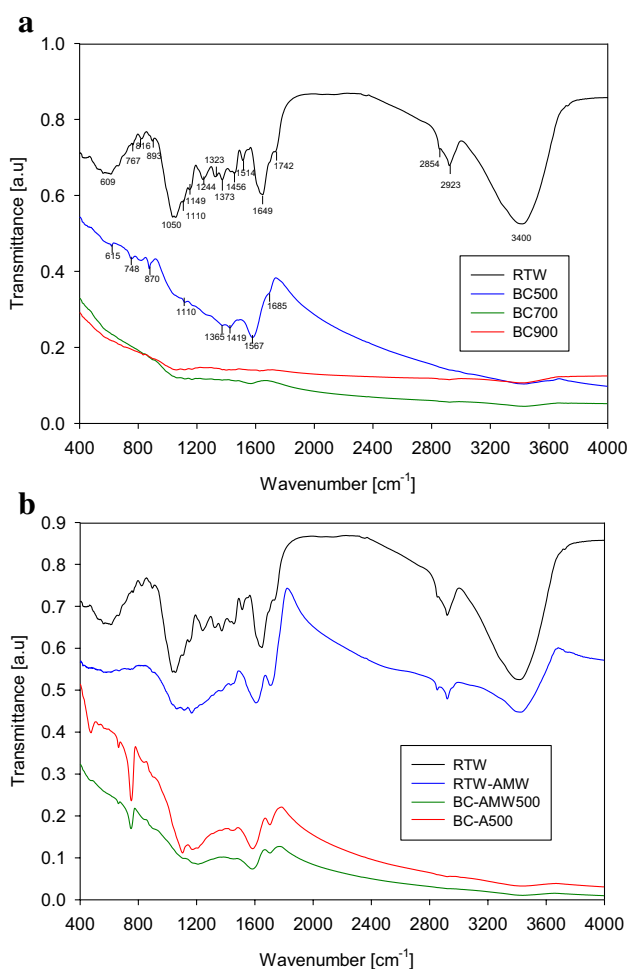


Fig. 7 **a** FT-IR spectra of RTW and biochars produced at varied temperatures. **b** FT-IR spectra of RTW and acid-activated biochars.

3.1.7 pH variation and pH_{pzc} determinations of samples

Table S3 lists surface pH and isoelectric point obtained by placing raw and pyrolyzed samples in water. RTW decreased the pH of neutral distilled water from 7.00 to 5.15, consistent with a surface bearing more acidic groups than basic groups [75]. Pyrolysis of RTW yielded samples that increased the pH of water that contacted them to extremely alkali levels, consistent with leaching of alkali salts exposed after pyrolysis [76–78]. Pyrolysis resulted in a negligible change in the point of zero charge (pH_{pzc}). The sample produced by acid promotion and MW activation decreased significantly the pH of contacting water, due to acid removal and the effect of surface acid functional groups.

The zeta potentials measured for RTW and biochars are shown in Fig. S3. RTW, and biochars have zeta potentials < -10 mV at pH values greater than 3.0, with the pH of surface neutrality at a pH between 1.5 and 2.0. Acid treatment results in particles with zeta potentials between 0 and -10 mV, again with the pH of surface neutrality at approximately 2.0. Acid-treated materials more closely balance anionic and cationic species than RTW or pyrolyzed materials, resulting in zeta potentials much closer to zero.

RTW and biochars contain oxygen-containing functional groups (e.g. $-\text{COO}^-$, $-\text{COH}$, $-\text{OH}$, and CO_3^{2-}) as seen in Fig. 7a. The presence of COO^- and OH^- on the biochar surface strongly influences their surface charge. Pyrolysis decreases or completely removes even these groups, shifting the zeta-potential–pH curves to more positive values (Fig. S3). Similarly, the MW activation and acid-promoted pyrolysis of RTW shifted zeta potential–pH curves to the positive region.

3.2 Metal adsorption characteristics of samples

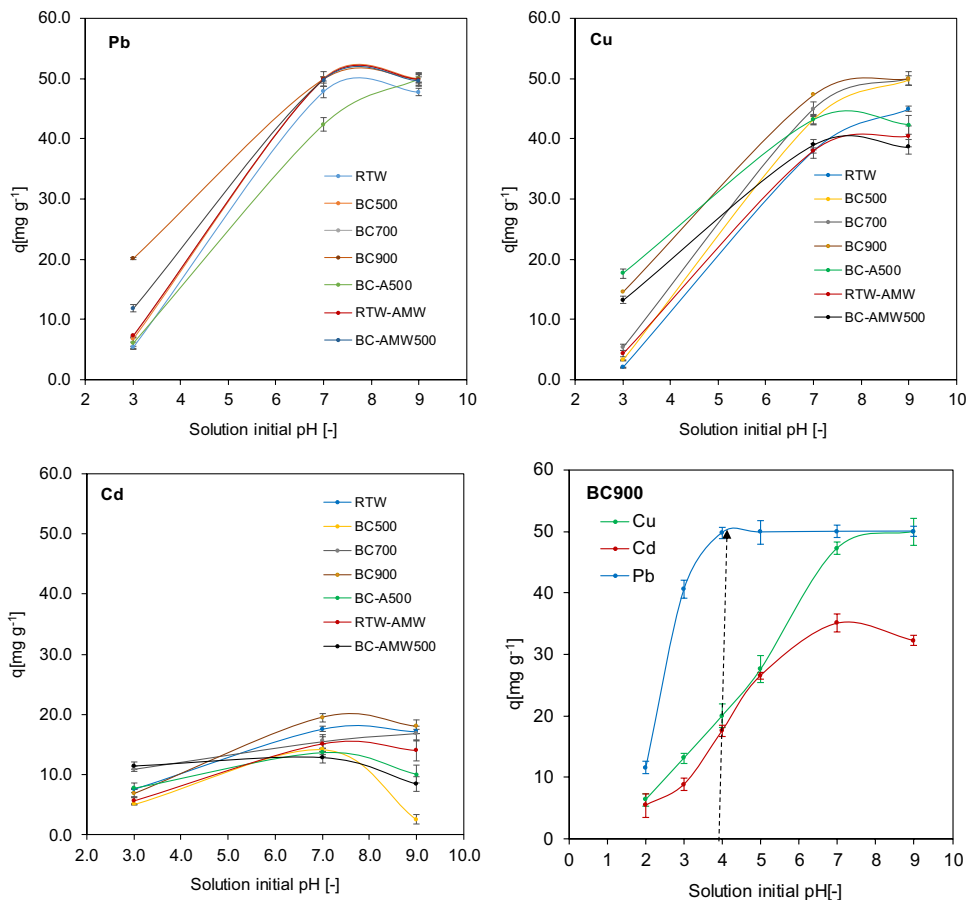
To evaluate the adsorption performance of the RTW, biochars, and acid-activated biochars, their adsorption capacities were tested for the uptake of Cd^{2+} , Cu^{2+} , and Pb^{2+} ions from aqueous solutions at three different initial solution pH values, and obtained results were shown in Fig. 8. At pH = 3.0, the adsorption capacities of the RTW and biochar samples for Cd^{2+} , Cu^{2+} , and Pb^{2+} are low. When the pH is increased from 3.0 to 7.0, their adsorption capacities increase. Low adsorption capacity at lower pH was reported by numerous studies [79, 80].

The effect of solution pH on adsorption capacity is mainly due to protonation or hydroxylation of the biochar surface.

Namely, the abundance H^+ ions at lower pH leads to a more highly positively charged surface, resulting in electrostatic repulsion between $\text{Cu}(\text{II})$, $\text{Cd}(\text{II})$, and $\text{Pb}(\text{II})$ ions and biochar surfaces. When the pH of the solution increases, acidic functional groups on the RTW and biochar surfaces deprotonate, resulting in more negatively charged surfaces desired for adsorption of positively charged metal ions [80].

The other mechanism for removal of $\text{Cu}(\text{II})$, and $\text{Pb}(\text{II})$ ions is hydroxylation of ions in the form $\text{Cd}(\text{OH})^+$, $\text{Cu}(\text{OH})^+$, and $\text{Pb}(\text{OH})^+$ when pH increases from 3.0 to 7.0, resulting in precipitation of metals on the surface [81]. $\text{Cu}(\text{II})$ and $\text{Pb}(\text{II})$ start precipitating at solution $\text{pH} \geq 5.8$ [82]. For this reason, the initial pH for adsorption studies of $\text{Cu}(\text{II})$ and $\text{Pb}(\text{II})$ was determined as pH 4. However, Cd^{2+} mostly forms of $\text{Cd}(\text{II})$ in the aqueous solution at $\text{pH} < 7.5$, and $\text{Cd}(\text{OH})^+$ begins to appear at $\text{pH} > 7.5$ [83]. $\text{Cd}(\text{OH})_2(\text{aq})$ was estimated to precipitate at $\text{pH} > 8.5$. Thus, to investigate the effect of pH on the adsorption of $\text{Cd}(\text{II})$, pH 7 was chosen to avoid the disturbance of $\text{Cd}(\text{OH})_2(\text{aq})$ [83]. Further increasing pH from 7.0 to 9.0 increases Cu capacity, decreases Cd capacity, and did not affect Pb capacity. Similar trends between solution pH and metal removal capacity are observed for biochars irrespective of pyrolysis temperature.

Fig. 8 Variation of adsorption capacity of samples as a function of solution initial pH [$T = 25^\circ\text{C}$; initial metal concentration = 50 mg L^{-1} ; adsorbent amount = 1 g/L ; contacting time = 6 h]



BC900 had the greatest adsorption capacity of all of the samples tested here (Fig. 8). This result might be related to its basic characteristic and slightly higher surface area. Therefore, a detailed pH study for BC900 was performed, subject to the restrictions of cation stability with respect to pH. Figure 8 summarizes the results. Maximum removal capacity values for BC900 were obtained at pH = 4.0 for Pb^{2+} and pH 7.0 of Cu^{2+} and Cd^{2+} .

For the most part, adsorption capacities provided in Fig. 8 are comparable to previous reports [84–86]. However, the Cd adsorption capacity of biochars produced at 500 and 700 °C is greater than that reported by Fan and Zhang (2019), which may be due to differences in the adsorption and pyrolysis operation conditions between the two studies. As a general rule, the metal capacity of biochars increased with increasing pyrolysis temperature, which can be seen by comparison of BC500, BC700, and BC900 in Fig. 8. The effect of pyrolysis temperature on adsorption capacity must be attributable to chemical effects since pyrolysis modestly increases BC surface area (see Table 2). Instead, the effect of pyrolysis may be to remove components (e.g., moisture evaporation, devolatilization, fragmentation) from RTW that are ineffective adsorbents, exposing more active surface area—or that the carbonaceous surface of the BC is preferred for heavy metal adsorption compared with the more chemically complex RTW surface (see especially Figs. 3 and 4a).

Activation typically increases the sorption capacity of RTW, and the magnitude of the effect depends on the metal ion, pH of adsorption, and the activation treatment. Acid activation is especially effective at increasing the adsorption capacity of Cu, as seen by a comparison of BC-A500 with RTW and BC900. The sorption capacity of BC-A500 is superior to BC900, despite the 400 °C difference in activation temperature (500 vs 900 °C). Acid-promoted microwave treatment is most effective for increasing Pb and Cu capacity, as seen by a comparison of BC-AMW500 with RTW and BC900. The superior performance of the acid and MW activated materials compared with the pyrolysis chars is readily attributable to the aforementioned differences in surface areas (see Table 2). The fact that adsorption capacity does not increase proportionally with surface area indicates the importance of surface chemistry—as well as surface area—for determining adsorption capacity.

The data in Fig. 8 suggest that activation of RTW can be tailored to achieve some selectivity for the removal of a desired metal or family of metals. For non-selective metal removal, combinations of adsorbents can be used—for example, a combined bed consisting of BC-AMW500 and BC-A500 for effective sorption of Pb, Cu, and Cd. To provide a rational basis for combining adsorbents, the adsorption mechanism was studied using spectroscopic

techniques, by investigating competitive adsorption, and by measuring adsorption rates.

3.3 Adsorbate-adsorbent interactions

FT-IR was used to shed light on the adsorption mechanism of metals to BC900, as shown in Fig. S4. Cd adsorption decreased density of $-\text{OH}$ and $-\text{CH}$ groups appeared at $3400\text{--}3500\text{ cm}^{-1}$ and 1456 cm^{-1} . C-H peak observed at 870 cm^{-1} decreased with Cd adsorption, and above 7.2 mg Cd/g sorbent, the peak disappeared. Methyl C-H stretching compounds in 2850 and 2920 cm^{-1} decreased after higher Cd sorption (27.0 mg g^{-1}). Harvey et al. reported that heavy metals can be adsorbed to an oxygen-free biochar surface by delocalized π electrons from $\gamma\text{-CH}$ and C=C [87]. In addition, the C-O peak detected at 1038 cm^{-1} shifted towards 1064 cm^{-1} with increasing Cd adsorption as seen in Fig. S4a. The wide peak between 1390 and 1600 cm^{-1} related with C=C decreased with increasing Cd adsorption. These findings are in accordance with the different biochar studies reported in the literature [40, 88–91]. Combined with all results and compared with literature, the proposed mechanism for Cd^{2+} adsorption by BC900 includes ion exchange ($\text{Cd}^{2+} + \text{CaSO}_4 \rightarrow \text{CdSO}_4 + \text{Ca}^{2+}$), chemical precipitation ($\text{Cd}^{2+} + \text{CO}_3^{2-} \rightarrow \text{CdCO}_3$), and complexation reaction of Cd^{2+} with oxygen-containing functional groups ($\text{Cd}_2\text{O}(\text{OH})_2$; Cd-COOH).

FT-IR spectrum in Fig. S4b shows that Cu adsorption led to disappear the peaks at 873 and 1380 cm^{-1} and a decrease the peaks at 1038 cm^{-1} , 1421 cm^{-1} , 2851 cm^{-1} , 2920 cm^{-1} , 3450 cm^{-1} , and 3520 cm^{-1} depending on Cu sorption amount. These results showed a complexation reaction between Cu^{2+} and functional groups of $-\text{OH}$, $-\text{CH}$, and $-\text{COOH}$. Similar results were reported for various biochar samples such as peanut straw char, soybean straw char, canola straw char, glucose hydrochar [92], black carbon derived from wheat residues [93], biochar derived from pistachio green hull [94], halophyte biochar [95], and woodchip-derived biochar [96].

Pb adsorption showed similar changes of functional groups of the biochar with Cd and Cu as seen in Fig. S4c. Prior studies indicated that ion exchange, electrostatic attraction, precipitation or co-precipitation, surface complexation with functional groups, and physical adsorption may contribute to heavy metals absorption on biochar [97, 98]. Based on zeta potential (Fig. S3), FT-IR (Fig. S4), and SEM-EDS (Fig. S5), the adsorption mechanism of Pb^{2+} and Cu^{2+} on biochar mostly involves precipitation with minor contributions possible from the other mechanisms. Cd^{2+} removal mainly occurs due to complexation between the cation and oxygen-containing functional groups.

To determine if the change of functional groups is coming from metal-functional groups' interaction or dissolution

of functional groups, total organic carbon of supernatant was determined. Total organic carbon amount after adsorption at pH 4.0 and pH 7.0 was determined as 51 ppm and 52 ppm, respectively. It indicates that solution pH affects insignificantly dissolution of carbon. In addition, a decrease in the carbon content of the biochar after metal sorption is not detected in the elemental analysis shown in Table 1.

3.4 Competitive adsorption

Heavy metals often coexist in contaminated wastewater systems, and their competitive behavior could affect the adsorption capacity of biochar. To explore the competitive behavior, a mixture of Pb^{2+} , Cu^{2+} , and Cd^{2+} was prepared at pH 4, and adsorption on BC900 was evaluated. Results are shown in Fig. S6. The biochar exhibited much greater adsorption capacity for Pb^{2+} , compared with Cu^{2+} and Cd^{2+} , suggesting that Pb has much greater affinity toward biochar than other metals. The maximum adsorption capacity for Pb^{2+} (6.0 mg g^{-1}) was obtained at the initial metal concentration of 50 mg L^{-1} . These results indicate that Pb will be preferentially removed before Cu and Cd, suggesting that a sequential bed should be designed to first remove this metal so that the others can then be removed. Adsorption capacity and SEM–EDS results showed that the affinity to Cd of BC900 follows Pb ions. The lowest adsorption capacity of BC900 was found as 3.5 mg/g for Cu. Compared with single metal adsorption results, affinity of BC900 to Cu replaced with Cd, which might be due to adsorption of Pb and Cd in the same activity sides. The affinity sequence of $\text{Pb} > \text{Cd} > \text{Cu}$ agrees with various biochar studies such as activated wood biochar [99], activated bone biochar [100], and wood derived biochar.

3.5 Adsorption kinetics

Adsorption rates of Pb^{2+} , Cd^{2+} , and Cu^{2+} on BC900 were measured for different initial metal concentrations at a constant adsorbent charge (1 g L^{-1}) at $25 \text{ }^\circ\text{C}$. Kinetic parameters for each of these three metals were calculated from adsorption measurements over time (shown in Fig. S7), and the parameters calculated are summarized in Table S5. Based on the correlation coefficients (R^2) in Table S4, a pseudo-second-order adsorption model captured the observed behavior, indicating that adsorption rate is likely controlled by chemisorption [101]. The rate constant k_2 for metal adsorption observed for BC900 followed the trend: $\text{Cd}^{2+} > \text{Cu}^{2+} > \text{Pb}^{2+}$, consistent with the aforementioned trend in their adsorption capacities. Moreover, trends in observed the adsorption rates and capacities do not follow from trends in hydrated ionic radius (Cd^{2+} (4.26 \AA) $>$ Cu^{2+} (4.19 \AA) $>$ Pb^{2+} (4.01 \AA)) [102]. Instead, trends in adsorption capacity and especially

rate are indicative of chemisorption limiting phenomena, rather than diffusion-limited behavior [103].

4 Conclusion

Biochars derived from raw tea waste (RTW) were produced under different pyrolysis conditions. Pyrolysis increased the carbon content and surface area of RTW. Addition of H_3PO_4 during pyrolysis led to formation of oxygen functional groups on the resulting char. Microwave activation in phosphoric acid significantly increased the number of micropores of biochar and led to a significant increase in the surface area of biochar. Biochar produced by pyrolysis of RTW at $900 \text{ }^\circ\text{C}$ exhibited the greatest Pb^{2+} capacity. On the other hand, the greatest Cu^{2+} and Cd^{2+} adsorption capacities were found on the biochars pyrolyzed in the presence of phosphoric acid, which is attributable to the abundance of various oxygen-containing functional groups and differences in adsorption mechanisms for the different metals. FT-IR analysis of metal impregnated chars revealed specific metal-char interactions, suggesting at least partial chemisorption to the surface. In all cases, metal uptake was best described by a pseudo-second-order kinetic model, supporting the conclusion of chemisorption limited uptake. These results provide new insight into the use of RTW for environmental applications.

Supplementary Information The online version contains supplementary material available at <https://doi.org/10.1007/s13399-021-01721-5>.

Funding The Sivas Cumhuriyet University research fund supported this work (M-784 and M-657). MTT thanks the U.S. National Science Foundation (ENG/CBET 1605916) for supporting his contribution.

References

- Hung CY, Tsai WT, Chen JW et al (2017) Characterization of biochar prepared from biogas digestate. *Waste Manag* 66:53–60. <https://doi.org/10.1016/j.wasman.2017.04.034>
- Sekar M, Mathimani T, Alagumalai A et al (2021) A review on the pyrolysis of algal biomass for biochar and bio-oil – bottlenecks and scope. *Fuel* 283:119190. <https://doi.org/10.1016/j.fuel.2020.119190>
- Das SK, Ghosh GK, Avasthe R (2020) Valorizing biomass to engineered biochar and its impact on soil, plant, water, and microbial dynamics: a review. *Biomass Convers Biorefinery* 1–17. <https://doi.org/10.1007/s13399-020-00836-5>
- Bartoli M, Rosi L, Giovannelli A et al (2016) Pyrolysis of α -cellulose using a multimode microwave oven. *J Anal Appl Pyrolysis* 120:284–296. <https://doi.org/10.1016/j.jaap.2016.05.016>
- Kumar Das S, Kumar Ghosh G, Avasthe R (2021) Applications of biomass derived biochar in modern science and technology. *Environ Technol Innov* 21:101306. <https://doi.org/10.1016/j.eti.2020.101306>

6. Kwak J-H, Islam MS, Wang S et al (2019) Biochar properties and lead(II) adsorption capacity depend on feedstock type, pyrolysis temperature, and steam activation. *Chemosphere* 231:393–404. <https://doi.org/10.1016/j.chemosphere.2019.05.128>
7. Qambrani NA, Rahman MM, Won S et al (2017) Biochar properties and eco-friendly applications for climate change mitigation, waste management, and wastewater treatment: a review. *Renew Sustain Energy Rev* 79:255–273. <https://doi.org/10.1016/j.rser.2017.05.057>
8. Wang B, Jiang Y, song, Li F yun, Yang D yue, (2017) Preparation of biochar by simultaneous carbonization, magnetization and activation for norfloxacin removal in water. *Bioresour Technol* 233:159–165. <https://doi.org/10.1016/j.biortech.2017.02.103>
9. Islam MA, Benhouria A, Asif M, Hameed BH (2015) Methylene blue adsorption on factory-rejected tea activated carbon prepared by conjunction of hydrothermal carbonization and sodium hydroxide activation processes. *J Taiwan Inst Chem Eng* 52:57–64. <https://doi.org/10.1016/j.jtice.2015.02.010>
10. Contreras MS, Páez CA, Zubizarreta L et al (2010) A comparison of physical activation of carbon xerogels with carbon dioxide with chemical activation using hydroxides. *Carbon N Y* 48:3157–3168. <https://doi.org/10.1016/j.carbon.2010.04.054>
11. Arami-Niya A, Daud WMAW, Mjalli FS (2011) Comparative study of the textural characteristics of oil palm shell activated carbon produced by chemical and physical activation for methane adsorption. *Chem Eng Res Des* 89:657–664. <https://doi.org/10.1016/j.cherd.2010.10.003>
12. Li B, Yang L, Wang C, quan, et al (2017) Adsorption of Cd(II) from aqueous solutions by rape straw biochar derived from different modification processes. *Chemosphere* 175:332–340. <https://doi.org/10.1016/j.chemosphere.2017.02.061>
13. Yargicoglu EN, Sadasivam BY, Reddy KR, Spokas K (2015) Physical and chemical characterization of waste wood derived biochars. *Waste Manag* 36:256–268. <https://doi.org/10.1016/j.wasman.2014.10.029>
14. Li K, Zheng Z, Li Y (2010) Characterization and lead adsorption properties of activated carbons prepared from cotton stalk by one-step H₃PO₄ activation. *J Hazard Mater* 181:440–447. <https://doi.org/10.1016/j.jhazmat.2010.05.030>
15. Cao L, Yu IKM, Tsang DCW et al (2018) Phosphoric acid-activated wood biochar for catalytic conversion of starch-rich food waste into glucose and 5-hydroxymethylfurfural. *Bioresour Technol* 267:242–248. <https://doi.org/10.1016/j.biortech.2018.07.048>
16. Chu G, Zhao J, Huang Y et al (2018) Phosphoric acid pretreatment enhances the specific surface areas of biochars by generation of micropores. *Environ Pollut* 240:1–9. <https://doi.org/10.1016/j.envpol.2018.04.003>
17. Fernandez ME, Ledesma B, Román S et al (2015) Development and characterization of activated hydrochars from orange peels as potential adsorbents for emerging organic contaminants. *Bioresour Technol* 183:221–228. <https://doi.org/10.1016/j.biortech.2015.02.035>
18. Wu Y, Cha L, Fan Y et al (2017) Activated biochar prepared by pomelo peel using H₃PO₄ for the adsorption of hexavalent chromium: performance and mechanism. *Water Air Soil Pollut* 228:405. <https://doi.org/10.1007/s11270-017-3587-y>
19. Taha SM, Amer ME, Elmarsafy AE, Elkady MY (2014) Adsorption of 15 different pesticides on untreated and phosphoric acid treated biochar and charcoal from water. *J Environ Chem Eng* 2:2013–2025. <https://doi.org/10.1016/j.jece.2014.09.001>
20. Miura M, Kaga H, Sakurai A et al (2004) Rapid pyrolysis of wood block by microwave heating. *J Anal Appl Pyrolysis* 71:187–199. [https://doi.org/10.1016/S0165-2370\(03\)00087-1](https://doi.org/10.1016/S0165-2370(03)00087-1)
21. Huang YF, Chiueh PT, Lo SL (2016) A review on microwave pyrolysis of lignocellulosic biomass. *Sustain Environ Res* 26(3):103–109. <https://doi.org/10.1016/j.serj.2016.04.012>
22. Wan Y, Chen P, Zhang B et al (2009) Microwave-assisted pyrolysis of biomass: catalysts to improve product selectivity. *J Anal Appl Pyrolysis* 86:161–167. <https://doi.org/10.1016/j.jaap.2009.05.006>
23. Hu X, jiang, Wang J song, Liu Y guo, et al (2011) Adsorption of chromium (VI) by ethylenediamine-modified cross-linked magnetic chitosan resin: Isotherms, kinetics and thermodynamics. *J Hazard Mater* 185:306–314. <https://doi.org/10.1016/j.jhazmat.2010.09.034>
24. Yagmur E, Ozmak M, Aktas Z (2008) A novel method for production of activated carbon from waste tea by chemical activation with microwave energy. *Fuel* 87:3278–3285. <https://doi.org/10.1016/j.fuel.2008.05.005>
25. İzgi MS, Saka C, Baytar O et al (2019) Preparation and characterization of activated carbon from microwave and conventional heated almond shells using phosphoric acid activation. *Anal Lett*. <https://doi.org/10.1080/00032719.2018.1495223>
26. Xing X, Jiang W, Li S et al (2019) Preparation and analysis of straw activated carbon synergetic catalyzed by ZnCl₂-H₃PO₄ through hydrothermal carbonization combined with ultrasonic assisted immersion pyrolysis. *Waste Manag* 89:64–72. <https://doi.org/10.1016/j.wasman.2019.04.002>
27. Villota SM, Lei H, Villota E et al (2019) Microwave-assisted activation of waste cocoa pod husk by H₃PO₄ and KOH - comparative insight into textural properties and pore development. *ACS Omega*. <https://doi.org/10.1021/acsomega.8b03514>
28. Peiris C, Nayanathara O, Navarathna CM et al (2019) The influence of three acid modifications on the physicochemical characteristics of tea-waste biochar pyrolyzed at different temperatures: a comparative study. *RSC Adv* 9:17612–17622. <https://doi.org/10.1039/C9RA02729G>
29. Dieng H, Zawawi RBM, Yusof NISBM et al (2016) Green tea and its waste attract workers of formicine ants and kill their workers-implications for pest management. *Ind Crops Prod*. <https://doi.org/10.1016/j.indcrop.2016.05.019>
30. Akgül G, Iglesias D, Ocon P, Moreno Jiménez E (2019) Valorization of tea-waste biochar for energy storage. *BioEnergy Res* 12:1012–1020. <https://doi.org/10.1007/s12155-019-10025-6>
31. Uzun BB, Apaydin-Varol E, Ateş F et al (2010) Synthetic fuel production from tea waste: characterisation of bio-oil and biochar. *Fuel* 89:176–184. <https://doi.org/10.1016/j.fuel.2009.08.040>
32. Rajapaksha AU, Vithanage M, Zhang M et al (2014) Pyrolysis condition affected sulfamethazine sorption by tea waste biochars. *Bioresour Technol* 166:303–308. <https://doi.org/10.1016/j.biortech.2014.05.029>
33. Li J, Yu G, Pan L et al (2018) Study of ciprofloxacin removal by biochar obtained from used tea leaves. *J Environ Sci* 73:20–30. <https://doi.org/10.1016/j.jes.2017.12.024>
34. Mandal S, Sarkar B, Igalavithana AD et al (2017) Mechanistic insights of 2,4-D sorption onto biochar: influence of feedstock materials and biochar properties. *Bioresour Technol* 246:160–167. <https://doi.org/10.1016/j.biortech.2017.07.073>
35. Mayakaduwa SS, Vithanage M, Karunaratna A et al (2016) Interface interactions between insecticide carbofuran and tea waste biochars produced at different pyrolysis temperatures. *Chem Speciat Bioavailab* 28:110–118. <https://doi.org/10.1080/09542299.2016.1198928>
36. Keerthan S, Bhatnagar A, Mahatantila K et al (2020) Engineered tea-waste biochar for the removal of caffeine, a model compound in pharmaceuticals and personal care products (PPCPs), from aqueous media. *Environ Technol Innov* 19:100847. <https://doi.org/10.1016/j.eti.2020.100847>

37. Shen B, Tian L, Li F et al (2017) Elemental mercury removal by the modified bio-char from waste tea. *Fuel* 187:189–196. <https://doi.org/10.1016/j.fuel.2016.09.059>
38. Roy S, Sengupta S, Manna S, Das P (2018) Chemically reduced tea waste biochar and its application in treatment of fluoride containing wastewater: batch and optimization using response surface methodology. *Process Saf Environ Prot* 116:553–563. <https://doi.org/10.1016/j.psep.2018.03.009>
39. Akgül G, Maden TB, Diaz E, Jiménez EM (2019) Modification of tea biochar with Mg, Fe, Mn and Al salts for efficient sorption of PO₄³⁻ and Cd²⁺ from aqueous solutions. *J Water Reuse Desalin* 9:57–66. <https://doi.org/10.2166/wrd.2018.018>
40. Fan S, Zhang L (2019) Production and characterization of tea waste-based biochar and its application in treatment of Cd-containing wastewater. *Biomass Convers Biorefinery* 1–13. <https://doi.org/10.1007/s13399-019-00545-8>
41. Pal D, Maiti SK (2019) Abatement of cadmium (Cd) contamination in sediment using tea waste biochar through meso-microcosm study. *J Clean Prod* 212:986–996. <https://doi.org/10.1016/j.jclepro.2018.12.087>
42. Serdar G, Demir E, Sökmen M (2017) Recycling of tea waste: simple and effective separation of caffeine and catechins by microwave assisted extraction (MAE). *Int J Second Metab* 4(2):78–89. <https://doi.org/10.21448/ijsm.288226>
43. Ahmad M, Rajapaksha AU, Lim JE et al (2014) Biochar as a sorbent for contaminant management in soil and water: a review. *Chemosphere* 99:19–33
44. Uchimiya M, Chang SC, Klasson KT (2011) Screening biochars for heavy metal retention in soil: role of oxygen functional groups. *J Hazard Mater* 190:432–441. <https://doi.org/10.1016/j.jhazmat.2011.03.063>
45. Ren Q, Zhao C, Chen X et al (2011) NO_x and N₂O precursors (NH₃ and HCN) from biomass pyrolysis: Co-pyrolysis of amino acids and cellulose, hemicellulose and lignin. *Proc Combust Inst* 33:1715–1722. <https://doi.org/10.1016/j.proci.2010.06.033>
46. Liu Q, Wang S, Zheng Y et al (2008) Mechanism study of wood lignin pyrolysis by using TG–FTIR analysis. *J Anal Appl Pyrolysis* 82:170–177. <https://doi.org/10.1016/j.jaap.2008.03.007>
47. Van Krevelen DW, Hermans PH, Schuyer J (1957) Coal science: aspects of coal constitution. Elsevier Publishing Company
48. Bakshi S, Banik C, Laird DA (2020) Estimating the organic oxygen content of biochar. *Sci Rep* 10:13082. <https://doi.org/10.1038/s41598-020-69798-y>
49. Chen D, Yu X, Song C et al (2016) Effect of pyrolysis temperature on the chemical oxidation stability of bamboo biochar. *Bioresour Technol* 218:1303–1306. <https://doi.org/10.1016/j.biortech.2016.07.112>
50. Sych NV, Trofymenko SI, Poddubnaya OI et al (2012) Porous structure and surface chemistry of phosphoric acid activated carbon from corncob. *Appl Surf Sci* 261:75–82. <https://doi.org/10.1016/j.apsusc.2012.07.084>
51. S R, Lata S, P B, (2018) Biosorption characteristics of methylene blue and malachite green from simulated wastewater onto Carica papaya wood biosorbent. *Surfaces and Interfaces* 10:197–215. <https://doi.org/10.1016/j.surfin.2017.09.011>
52. Lopičić ZR, Stojanović MD, Marković SB et al (2019) Effects of different mechanical treatments on structural changes of lignocellulosic waste biomass and subsequent Cu(II) removal kinetics. *Arab J Chem* 12:4091–4103. <https://doi.org/10.1016/j.arabjc.2016.04.005>
53. Selvasembian R, Balasubramanian P (2018) Utilization of unconventional lignocellulosic waste biomass for the biosorption of toxic triphenylmethane dye malachite green from aqueous solution. *Int J Phytoremediation* 20:624–633. <https://doi.org/10.1080/15226514.2017.1413329>
54. Peng C, Bin YX, Wang RT et al (2013) Promising activated carbons derived from waste tea-leaves and their application in high performance supercapacitors electrodes. *Electrochim Acta* 87:401–408. <https://doi.org/10.1016/j.electacta.2012.09.082>
55. Prahas D, Kartika Y, Indraswati N, Ismadji S (2008) Activated carbon from jackfruit peel waste by H₃PO₄ chemical activation: pore structure and surface chemistry characterization. *Chem Eng J* 140:32–42. <https://doi.org/10.1016/j.cej.2007.08.032>
56. Liu HY, Wang KP, Teng H (2005) A simplified preparation of mesoporous carbon and the examination of the carbon accessibility for electric double layer formation. *Carbon N Y* 43:559–566. <https://doi.org/10.1016/j.carbon.2004.10.020>
57. Rey-Raap N, Menéndez JA, Arenillas A (2014) Optimization of the process variables in the microwave-induced synthesis of carbon xerogels. *J Sol-Gel Sci Technol* 69:488–497. <https://doi.org/10.1007/s10971-013-3248-6>
58. Hoseinzadeh Hesas R, Wan Daud WMA, Sahu JN, Arami-Niya A (2013) The effects of a microwave heating method on the production of activated carbon from agricultural waste: a review. *J Anal Appl Pyrolysis* 100:1–11
59. Al Bahri M, Calvo L, Gilarranz MA, Rodriguez JJ (2012) Activated carbon from grape seeds upon chemical activation with phosphoric acid: application to the adsorption of diuron from water. *Chem Eng J* 203:348–356. <https://doi.org/10.1016/j.cej.2012.07.053>
60. Lin Y, Munroe P, Joseph S et al (2012) Water extractable organic carbon in untreated and chemical treated biochars. *Chemosphere* 87:151–157. <https://doi.org/10.1016/j.chemosphere.2011.12.007>
61. Patnukao P, Pavasant P (2008) Activated carbon from Eucalyptus camaldulensis Dehn bark using phosphoric acid activation. *Bioresour Technol* 99:8540–8543. <https://doi.org/10.1016/j.biortech.2006.10.049>
62. Peng H, Gao P, Chu G et al (2017) Enhanced adsorption of Cu(II) and Cd(II) by phosphoric acid-modified biochars. *Environ Pollut* 229:846–853. <https://doi.org/10.1016/j.envpol.2017.07.004>
63. Myglovets M, Poddubnaya OI, Sevastyanova O et al (2014) Preparation of carbon adsorbents from lignosulfonate by phosphoric acid activation for the adsorption of metal ions. *Carbon N Y* 80:771–783. <https://doi.org/10.1016/j.carbon.2014.09.032>
64. Sun X, Cheng P, Wang H et al (2015) Activation of graphene aerogel with phosphoric acid for enhanced electrocapacitive performance. *Carbon N Y* 92:1–10. <https://doi.org/10.1016/j.carbon.2015.02.052>
65. Sun L, Li M, Ma C, Li P (2017) Preparation and evaluation of Jatropha curcas based catalyst and functionalized blend components for low sulfur diesel fuel. *Fuel* 206:27–33. <https://doi.org/10.1016/j.fuel.2017.05.093>
66. Boumanchar I, Chhiti Y, M'hamdi Alaoui FE, et al (2017) Effect of materials mixture on the higher heating value: case of biomass, biochar and municipal solid waste. *Waste Manag* 61:78–86. <https://doi.org/10.1016/j.wasman.2016.11.012>
67. Shen DK, Gu S (2009) The mechanism for thermal decomposition of cellulose and its main products. *Bioresour Technol* 100:6496–6504. <https://doi.org/10.1016/j.biortech.2009.06.095>
68. Jia Y, Lu Y, Zhang G et al (2017) Facile synthesis of an eco-friendly nitrogen–phosphorus ammonium salt to enhance the durability and flame retardancy of cotton. *J Mater Chem A* 5:9970–9981. <https://doi.org/10.1039/C7TA01106G>
69. Yang H, Yan R, Chen H et al (2007) Characteristics of hemicellulose, cellulose and lignin pyrolysis. *Fuel* 86(12–13):1781–1788. <https://doi.org/10.1016/j.fuel.2006.12.013>
70. Weber K, Quicker P (2018) Properties of biochar. *Fuel* 217:240–261. <https://doi.org/10.1016/j.fuel.2017.12.054>
71. Pandey KK, Pitman AJ (2003) FTIR studies of the changes in wood chemistry following decay by brown-rot and white-rot

- fungi. *Int Biodeterior Biodegrad* 52:151–160. [https://doi.org/10.1016/S0964-8305\(03\)00052-0](https://doi.org/10.1016/S0964-8305(03)00052-0)
72. Naumann A, Navarro-González M, Peddireddi S et al (2005) Fourier transform infrared microscopy and imaging: detection of fungi in wood. *Fungal Genet Biol* 42:829–835. <https://doi.org/10.1016/j.fgb.2005.06.003>
 73. Novak J, Lima I, Xing B et al (2009) Characterization of designer biochar produced at different temperatures and their effects on a loamy sand. *Ann Environ Sci* 3:195–206. <http://hdl.handle.net/2047/d10019637>
 74. Li X, Shen Q, Zhang D et al (2013) Functional groups determine biochar properties (pH and EC) as studied by two-dimensional ^{13}C NMR correlation spectroscopy. *Plos One* 8(6):1–7. <https://doi.org/10.1371/journal.pone.0065949>
 75. Mestre AS, Pires J, Nogueira JMF, Carvalho AP (2007) Activated carbons for the adsorption of ibuprofen. *Carbon N Y* 45:1979–1988. <https://doi.org/10.1016/j.carbon.2007.06.005>
 76. Yuan JH, Xu RK, Zhang H (2011) The forms of alkalis in the biochar produced from crop residues at different temperatures. *Bioresour Technol* 102:3488–3497. <https://doi.org/10.1016/j.biortech.2010.11.018>
 77. Al-Wabel MI, Al-Omran A, El-Naggar AH et al (2013) Pyrolysis temperature induced changes in characteristics and chemical composition of biochar produced from conocarpus wastes. *Bioresour Technol* 131:374–379. <https://doi.org/10.1016/j.biortech.2012.12.165>
 78. Gundogdu A, Duran C, Senturk HB et al (2013) Physicochemical characteristics of a novel activated carbon produced from tea industry waste. *J Anal Appl Pyrolysis* 104:249–259. <https://doi.org/10.1016/j.jaap.2013.07.008>
 79. Ahmad Z, Gao B, Mosa A et al (2018) Removal of Cu(II), Cd(II) and Pb(II) ions from aqueous solutions by biochars derived from potassium-rich biomass. *J Clean Prod* 180:437–449. <https://doi.org/10.1016/j.jclepro.2018.01.133>
 80. Ding Y, Liu Y, Liu S et al (2016) Competitive removal of Cd (II) and Pb (II) by biochars produced from water hyacinths: performance and mechanism. *RSC Adv* 6:5223–5232
 81. Wang H, Gao B, Wang S et al (2015) Removal of Pb(II), Cu(II), and Cd(II) from aqueous solutions by biochar derived from KMnO₄ treated hickory wood. *Bioresour Technol* 197:356–362. <https://doi.org/10.1016/j.biortech.2015.08.132>
 82. Tiwari D, Laldanwngliana C, Choi CH, Lee SM (2011) Manganese-modified natural sand in the remediation of aquatic environment contaminated with heavy metal toxic ions. *Chem Eng J* 171:958–966. <https://doi.org/10.1016/j.cej.2011.04.046>
 83. Liu P, Rao D, Zou L et al (2021) Capacity and potential mechanisms of Cd(II) adsorption from aqueous solution by blue algae-derived biochars. *Sci Total Environ* 767:145447. <https://doi.org/10.1016/j.scitotenv.2021.145447>
 84. Wan S, Ma Z, Xue Y et al (2014) Sorption of lead(II), cadmium(II), and copper(II) ions from aqueous solutions using tea waste. *Ind Eng Chem Res* 53:3629–3635. <https://doi.org/10.1021/ie402510s>
 85. Çay S, Uyanik A, Özaşık A (2004) Single and binary component adsorption of copper(II) and cadmium(II) from aqueous solutions using tea-industry waste. *Sep Purif Technol* 38:273–280. <https://doi.org/10.1016/j.seppur.2003.12.003>
 86. Amarasinghe BMWPK, Williams RA (2007) Tea waste as a low cost adsorbent for the removal of Cu and Pb from wastewater. *Chem Eng J* 132:299–309. <https://doi.org/10.1016/j.cej.2007.01.016>
 87. Harvey OR, Herbert BE, Rhue RD, Kuo LJ (2011) Metal interactions at the biochar-water interface: energetics and structure-sorption relationships elucidated by flow adsorption microcalorimetry. *Environ Sci Technol* 45:5550–5556. <https://doi.org/10.1021/es104401h>
 88. Xu X, Cao X, Zhao L et al (2013) Removal of Cu, Zn, and Cd from aqueous solutions by the dairy manure-derived biochar. *Environ Sci Pollut Res* 20:358–368. <https://doi.org/10.1007/s11356-012-0873-5>
 89. Bashir S, Zhu J, Fu Q, Hu H (2018) Comparing the adsorption mechanism of Cd by rice straw pristine and KOH-modified biochar. *Environ Sci Pollut Res* 25:11875–11883. <https://doi.org/10.1007/s11356-018-1292-z>
 90. Chang R, Sohi SP, Jing F et al (2019) A comparative study on biochar properties and Cd adsorption behavior under effects of ageing processes of leaching, acidification and oxidation. *Environ Pollut* 254:113123. <https://doi.org/10.1016/j.envpol.2019.113123>
 91. Zhang L, Ren Y, Xue Y et al (2020) Preparation of biochar by mango peel and its adsorption characteristics of Cd (II) in solution. *RSC Adv* 10:35878–35888. <https://doi.org/10.1039/D0RA06586B>
 92. Delahaye L, Hobson JT, Rando MP et al (2020) Experimental and computational evaluation of heavy metal cation adsorption for molecular design of hydrothermal char. *Energies* 13:4203. <https://doi.org/10.3390/en13164203>
 93. Wang XS, Miao HH, He W, Shen HL (2011) Competitive adsorption of Pb(II), Cu(II), and Cd(II) ions on wheat-residue derived black carbon. *J Chem Eng Data* 56:444–449. <https://doi.org/10.1021/je101079w>
 94. Jalayeri H, Pepe F (2019) Novel and high-performance biochar derived from pistachio green hull biomass: production, characterization, and application to Cu(II) removal from aqueous solutions. *Ecotoxicol Environ Saf* 168:64–71. <https://doi.org/10.1016/j.ecoenv.2018.10.058>
 95. Wei J, Tu C, Yuan G et al (2019) Assessing the effect of pyrolysis temperature on the molecular properties and copper sorption capacity of a halophyte biochar. *Environ Pollut* 251:56–65. <https://doi.org/10.1016/j.envpol.2019.04.128>
 96. Rechberger MV, Kloss S, Wang S-L et al (2019) Enhanced Cu and Cd sorption after soil aging of woodchip-derived biochar: what were the driving factors? *Chemosphere* 216:463–471. <https://doi.org/10.1016/j.chemosphere.2018.10.094>
 97. Usman A, Sallam A, Zhang M et al (2016) Sorption process of date palm biochar for aqueous Cd (II) removal: efficiency and mechanisms. *Water, Air, Soil Pollut* 227:449. <https://doi.org/10.1007/s11270-016-3161-z>
 98. Abdin Y, Usman A, Ok YS et al (2020) Competitive sorption and availability of coexisting heavy metals in mining-contaminated soil: contrasting effects of mesquite and fishbone biochars. *Environ Res* 181:108846. <https://doi.org/10.1016/j.envres.2019.108846>
 99. Namgay T, Singh B, Singh BP (2010) Influence of biochar application to soil on the availability of As, Cd, Cu, Pb, and Zn to maize (*Zea mays* L.). *Australian J Soil Res* 48(7):638–647. <https://doi.org/10.1071/SR10049>
 100. Xiao J, Hu R, Chen G (2020) Micro-nano-engineered nitrogenous bone biochar developed with a ball-milling technique for high-efficiency removal of aquatic Cd(II), Cu(II) and Pb(II). *J Hazard Mater* 387:121980. <https://doi.org/10.1016/j.jhazmat.2019.121980>
 101. Ho YS (2006) Review of second-order models for adsorption systems. *J Hazard Mater* 136:681–689. <https://doi.org/10.1016/j.jhazmat.2005.12.043>
 102. Lü L, Chen L, Shao W, Luo F (2010) Equilibrium and kinetic modeling of Pb(II) biosorption by a chemically modified orange peel containing Cyanex 272. *J Chem Eng Data* 55:4147–4153. <https://doi.org/10.1021/je1000846>
 103. Liang X, Zang Y, Xu Y et al (2013) Sorption of metal cations on layered double hydroxides. *Colloids Surfaces A Physicochem Eng Asp* 433:122–131

Publisher's note Springer Nature remains neutral with regard to jurisdictional claims in published maps and institutional affiliations.